An 8-yr meteotsunami climatology across northwest Europe: 2010–2017

DOI:
10.1175/JPO-D-20-0175.1

Document Version
Accepted author manuscript

An 8-yr meteotsunami climatology across northwest Europe: 2010–2017

David A Williams[1,4], David M Schultz[2], Kevin J Horsburgh[3], Chris W Hughes[1]

1 – Department of Earth, Ocean and Ecological Sciences, University of Liverpool, Liverpool, United Kingdom

2 – School of Earth and Environmental Sciences, University of Manchester, Manchester, United Kingdom

3 – National Oceanography Centre, Liverpool, United Kingdom

4 – Current affiliation: Willis Towers Watson, London, United Kingdom

Corresponding author: David Williams, davidwilliams0100@gmail.com

ABSTRACT

Meteotsunamis are shallow-water waves that, despite often being small (~ 0.3 m), can cause damage, injuries and fatalities due to relatively strong currents (> 1 m s^{-1}). Previous case studies, modelling and localised climatologies have indicated that dangerous meteotsunamis can occur across northwest Europe. Using 71 tide gauges across northwest Europe between 2010–2017, a regional climatology was made to understand the typical sizes, times and atmospheric systems that generate meteotsunamis. A total of 349 meteotsunamis (54.0 meteotsunamis per year) were identified with 0.27–0.40 m median wave heights. The largest waves (~ 1 m high) were measured in France and the Republic of Ireland. Most meteotsunamis were identified in winter (43–59%), and the fewest identified meteotsunamis occurred in either spring or summer (0–15%). There was a weak diurnal signal, with most meteotsunami identifications between 1200–1859 UTC (30%) and fewest between 0000–0659 UTC (23%). Radar-derived precipitation was used to identify and classify the morphologies of mesoscale precipitating weather systems occurring within 6 h of each meteotsunami. Most mesoscale atmospheric systems were quasi-linear systems (46%) or open-cellular convection (33%), with some non-linear clusters (17%) and a few isolated cells (4%). These systems occurred under westerly geostrophic flow, with Proudman resonance possible in 43 out of 45 selected meteotsunamis. Because most meteotsunamis occur on cold winter days, with precipitation, and in large tides, wintertime meteotsunamis may be missed by eyewitnesses, helping to explain why previous observationally-based case studies of meteotsunamis are documented predominantly in summer.

1. Introduction

Meteotsunamis are shallow-water waves with periods between 2–120 minutes that are generated by moving weather systems. The atmospheric pressure and wind fields associated with those weather systems can force wave growth, known as external resonance (e.g., Proudman 1929; Greenspan 1956; Monserrat et al. 2006; Vilibić 2008), which amplifies waves up to tens of centimetres (e.g., Orlić 1980; Hibiya and Kajiura 1982; Choi et al. 2014; Šepić et al. 2015a; Anderson et al. 2015; Ličer et al. 2017). External resonance occurs when atmospheric-system speeds match wave speeds, typically in regions of shallow (< 100 m), gently sloping (< 0.1 m km^{-1}) bathymetry. After growth through external resonance, meteotsunamis are amplified by refraction and shoaling (e.g., Monserrat et al. 2006). Meteotsunamis that grow through external resonance, refraction and shoaling are commonly 0.1–1 m high (peak to trough). However, when meteotsunamis result in an excitation of a seiche within a bay, the residual water levels can exceed 2 m. Meteotsunamis that seiche can cause flooding and millions of USD in damages (e.g., Monserrat et al. 2006; Vučetić et al. 2009; Rabinovich 2009; Orlić et al. 2010). However, even meteotsunamis with modest wave heights may produce dangerous currents. For example, a 0.3-m high meteotsunami produced rip currents in Lake Michigan on 4 July 2003 that drowned seven people (Linares et al. 2019).

Although meteotsunamis are sometimes dangerous, how common they are is generally unknown. A global climatology indicates that small non-seismic sea-level oscillations with tsunami timescales (NSLOTTs) are fairly common, contributing up to 50% of sea-level variance in basins with tidal ranges < 1 m (Vilibić and Šepić 2017). Table 1 includes other studies that have produced size-exceedance rates in regions prone to meteotsunamis, including the Mediterranean (e.g., Šepić et al. 2012; Šepić et al. 2015b) and US basins (e.g., Bechle et al. 2016; Olabarrieta et al. 2017; Dusek et al. 2019). In these places, a moderately large meteotsunami (~1 m) is expected once every few years. The biggest similarity between these regions is that they contain a large (~10^5 km^2) region of shallow, gently sloping bathymetry. However, a similarly large (6×10^5 km^2) region that is known for meteotsunamis has not been represented by a regional climatology—the northwest European continental shelf (Fig. 1).

Climatologies are useful because they quantify conditions during which meteotsunamis occur. These, in turn, allow testing of the scientific hypotheses about their occurrence, formation and amplification. For example, do meteotsunamis occur preferentially at particular times? If meteotsunamis were to occur mostly in the summer between 0700–1900 local time, beachgoers would be at greater risk than if meteotsunamis were to occur mostly in winter between 1900–0700 local time. In fact, historical case studies indicate that northwest European meteotsunamis mainly occur in summer without diurnal preference (e.g., Douglas 1929; Haslett et al. 2009; Tappin et al. 2013; Frère et al. 2014; Sibley et al. 2016; Williams et al. 2019; Thompson et al. 2020).

However, analyses of tide gauges over several years sometimes suggest the opposite seasonality. Analysis of the Southampton tide gauge on the south coast of the United Kingdom (UK), has indicated that large 3–5-h period waves typically occur in autumn and winter (Oszoy et al. 2016). Although not classified as meteotsunamis according to the definitions in this work, it seems reasonable to assume that meteotsunami seasonality (2 min – 2 h period) should not be considerably different to waves of atmospheric origin with a slightly longer period (3–5 h). Furthermore, a climatology of atmospherically-generated seiches in Rotterdam, which we interpret as meteotsunamis, also showed that most Dutch meteotsunamis occur in autumn and winter (e.g., de Jong and Battjes 2004). Clearly, there is discrepancy between the seasonality of meteotsunamis in case studies, and the suggested seasonality from localised climatologies (loosely referring to a long-term analysis of less than 10 tide gauges along a coastline).

Once the time of events are known, we can also link the conditions of their identified occurrence to concurrent atmospheric conditions. One question is whether meteotsunamis occur primarily with particular mesoscale weather systems. For example, meteotsunamis in the Great Lakes tend to be generated by fronts, linear convective systems and non-linear convective complexes rather than discrete, individual cells (e.g., Bechle et al. 2015, 2016). This result is consistent with idealised simulations indicating that linear pressure forcings are more likely to generate meteotsunamis than circular forcings with the same along-propagation wavelength (Williams et al. 2020).

Identifying meteotsunamis from observations can be difficult. To identify meteotsunamis, three steps are generally required. First, signals in the tsunami frequency band (2–120-min periods) are isolated from lower- and higher-frequency sea-level elevations. Second, waves that are significantly larger than background noise in the residual signal are identified. Third, it needs to be demonstrated that the waves are atmospherically generated. There are multiple valid choices when implementing these three steps. For example, 10 different approaches are present in Table 1.

To illustrate the variety of choices available within each step, consider valid choices in the second step — the amplitude threshold to distinguish waves from background noise. Previous studies have used a significant wave height relative to the de-tided residual noise (e.g., Bechle et al. 2015; Kim et al. 2016; Olabarrieta et al. 2017; Carvajal et al. 2017), an absolute wave-height threshold (e.g., de Jong and Battjes 2004; Šepić et al. 2012; Linares et al. 2016; Bechle et al. 2016), and a mix of both methods (e.g., Šepić et al. 2009; Dusek et al. 2019). These choices result in different detection rates of meteotsunamis, with lower-amplitude thresholds yielding more meteotsunamis.

In this article, we consider meteotsunamis in northwest Europe. Although numerous case studies of meteotsunamis and localised climatologies in northwest Europe have been published (e.g., de Jong and Battjes 2004; Haslett et al. 2009; Tappin et al. 2013; Frère et al. 2014; Oszoy et al. 2016; Sibley et al. 2016; Williams et al. 2019), a regional climatology that quantifies the average (i.e. median) and extreme wave heights, the identified occurrence time, and the associated atmospheric systems has not been constructed. Without size-exceedance rates, quantifying the hazard posed by meteotsunamis is not possible. The purpose of this article is to produce the first regional climatology of meteotsunamis for northwest Europe and identify the atmospheric phenomena that are associated with meteotsunamis. This northwest European climatology will answer how frequently meteotsunamis of certain wave heights occur (size-exceedance rates), when they occur (diurnal and seasonal variation), and which precipitating weather systems tend to co-occur with meteotsunamis. This climatology will also provide evidence to test the hypothesis that linear systems tend to generate meteotsunamis.

The structure of the rest of this article is as follows. In section 2, we describe the data, how NSLOTTs and meteotsunamis were detected from this data, and the atmospheric system classification scheme. Then, in section 3, we present results and discussion of the size-exceedance rates, seasonal and diurnal variation and atmospheric conditions. Finally, we conclude in section 4.

2. Data and methods

To produce a meteotsunami climatology, we linked NSLOTT identifications to precipitating atmospheric systems that were measured by radar and identified from pre-processed images (Met Office 2003). This section outlines the data and choices used in this study to define a meteotsunami.

a. Tide-gauge data

We used 90 tide gauges between 1 January 2010 – 31 December 2017 (Fig. 1). Overall, the median data completeness was 92%. The tide gauges were provided in intervals of 5 min in Belgium and the Republic of Ireland, 6 min in the Republic of Ireland, 10 min in France, the Netherlands and Germany, and 15 min in the UK. (Hereafter, the Republic of Ireland is referred to as 'Ireland'). Typically, a 1-min data interval is deemed the highest-quality data for meteotsunami wave height and size-exceedance rates (e.g., Kim et al. 2016; Vilibić and Šepić 2017; Carvajal et al. 2017; Dusek et al. 2019). Tide gauges with 1-min averaging intervals were available in all countries at some locations, but have not been used, partly because of the time it would take to process the 1-min data manually (i.e. methods described in sections 2b and 2c).

However, the data intervals should be short enough to identify meteotsunamis. In the US, 6-min data have been used in climatologies to quantify size-exceedance rates and determine seasonal variability (Bechle et al. 2016; Olabarrieta et al. 2017; Dusek et al. 2019). Furthermore, a climatology of relatively high-frequency waves (3–5-h periods) was constructed in the UK using 15-min averaging intervals (Oszoy et al. 2016). Therefore, we expected that 10-min and 15-min tide-gauge data could also be used to identify particularly large non-seismic sea-level oscillations at tsunami timescales (termed NSLOTTs as in Vilibić and Šepić (2017)). However, wave heights from these 10-min and 15-min datasets will likely be aliased and underestimate size-exceedance rates.

The tide gauges also covered different time periods. Data from Ireland, the UK and France were between Jan 2010 – Dec 2017, data from Belgium were between Jan 2010 – Dec 2016 and data from the Netherlands and Germany were between Oct 2014 – Dec 2017 (Copernicus download, Table 2). Data were removed when not covering a full year, eliminating bias towards any particular season in further analysis. Therefore, data between Oct 2014 – Dec 2014 were removed for the Netherlands and Germany. No corrections were made for missing data between January and December.

b. Isolating non-tidal waves with periods less than 120 minutes

First, any 120-min high-pass filtered data that had a magnitude greater than four times the standard deviation of the residual was visually inspected. Upon visual inspection, data were removed if corresponding to spikes, incorrect timings, missing-data replacement values, inappropriate absolute sea-level elevation or jumps in data.

After preliminary data cleaning, tidal components of the sea-level elevation and periods > 120 min were removed to isolate tsunami-period signals. The averaging intervals used here are 5–15 min and are unable to reliably show waves with periods less than 10–30 min, nor properly represent wave heights with periods less than 50–150 min. As the sea-level elevation had already been low-pass filtered (due to long intervals), we applied a fourth-order, zero-phase, 120-min high-pass Butterworth (1930) filter to retain signals with periods < 120 min.

However, this filter did not remove all unwanted tidal noise. After high-pass filtering, there were repeating wavelets with wave heights on the order of tens of centimetres (peak to trough) with periods of ~90 min. These repeating wavelets were identified in the data from most tide gauges. Autocorrelation of the sea-level elevation time series showed that the wavelets repeated in about 12-h 25-min intervals (i.e. M_2 periodicity). The wavelet amplitudes were also modulated over 28 days with the spring-neap cycle. The repeating wavelets could not be fully removed by first applying tidal harmonic analysis (U-tide in Python). Synthetic time series (M_2, M_4, M_6, and M_8 constituents) suggested that these repeating wavelets were damped higher-frequency tidal components.

Therefore, a stacking algorithm was designed to remove the mean repeating wavelet signal at 12-h 25-min intervals. A stacking correction was designed to remove unwanted tidal signals that high-pass filtering did not remove. First, the filtered time series were resampled at 1-minute intervals and separated into equal segments (e.g. 12-hr 25-min segments). Seven segments were consecutively taken, and the central (fourth segment) was taken to be the target segment. The correlation coefficient with the target segment and the six other segments (of which three were earlier in time, and three were later in time than the target segment) were calculated. The three segments with the largest correlation coefficients to the target segment were averaged, producing a mean segment. This mean segment was removed from the target segment, leaving a corrected residual. This was repeated for all segments, and the corrected residuals were chronologically recombined. Further information on the stacking algorithm is supplied in Appendix E of Williams (2020).

Performing this algorithm on synthetic data with four tidal coefficients suggested that the stacking algorithm could remove 94% of the tidal sea-level residual that was not removed by high-pass filtering. On the real data, the algorithm showed mixed success in suppressing wavelets, and in the worst cases did not suppress the wavelets at all during a spring-neap cycle. Therefore, peaks that were detected at the standard deviation of the signal, σ, multiplied by a factor of 6 (termed 6σ), were visually inspected. If the peak was part of the repeating wavelet cycle, it was removed. After this manual data processing, 71 out of the 90 tide gauges (79%) were accepted for further analysis (black outline and black text in Fig. 1).

c. NSLOTT classification

Significant wave events were distinguished from background noise using an amplitude threshold. Here, events passed the amplitude threshold with wave heights (peak to trough) greater than 6σ. Across individual tide gauges, the largest detection within a 36-h interval was then chosen, ensuring that reflections from a single event were not repeated.

The 6σ-event dataset was then cross-referenced with seismic events. Two 4.8 M_w earthquakes occurred in the North Sea, but neither occurred on days with 6σ events (taken from the Harvard Moment Tensor Catalog (Dziewoński et al. 1981; Ekström et al. 2012)).

Individual events were then grouped into NSLOTT events if they were identified at two or more tide gauges within a 3-h interval (the event interval). This event interval was deemed appropriate because of 10–100 km separations between tide gauges, 25–100 km h^{-1} shallow-water wave speeds, and because mesoscale atmospheric systems last a few hours. There was no imposed maximum time limit for an NSLOTT event, meaning that the event interval controlled the number of NSLOTT events. After this processing, the largest measured wave height in an NSLOTT event was set as the NSLOTT wave height.

d. Meteotsunami classification

1) AMPLITUDE THRESHOLD

An absolute wave-height threshold was then used to categorize high-amplitude NSLOTTs (e.g., Šepić et al. 2009; Šepić et al. 2012; Bechle et al. 2016). We used a 0.25-m threshold, which is between previously used 0.2 m (Dusek et al. 2019) and 0.3 m (Bechle et al. 2016) thresholds. Hereafter, an NSLOTT with an absolute wave-height threshold exceeding 0.25 m is called a high-amplitude NSLOTT.

From analysis on Belgian data, we suggest that because of aliasing effects on wave height, a 0.25-m threshold with 15-min averaging intervals results in about the same number of events as a 0.3-m threshold with 5-min averaging intervals. Exceeding this 0.25-m wave-height threshold was not sufficient condition to classify an NSLOTT as a meteotsunami, which also required linking the event to a weather system.

2) IDENTIFYING A COINCIDENT ATMOSPHERIC SYSTEM

To classify NSLOTTs as meteotsunamis, events needed to be linked to a corresponding precipitating weather feature. Although meteotsunamis are created by moving atmospheric surface pressure gradients and surface wind stresses, dense measurement networks to identify possible meteotsunami-generating atmospheric features over the water are unavailable. Thus, we resort to remotely-sensed data to identify atmospheric features.

Specifically, weather radar can be used to remotely sense atmospheric precipitation-sized particles. As precipitating weather features are commonly associated with horizontal pressure gradients (e.g., Johnson 2001), such features can also be associated with meteotsunamis (e.g., Wertman et al. 2014). We expected that a minority of meteotsunamis would have been generated by non-precipitating forcings, because all previous northwest European studies indicate precipitating weather features associated with meteotsunamis (e.g., de Jong and Battjes 2004; Haslett et al. 2009; Tappin et al. 2013; Frère et al. 2014; Sibley et al. 2016; Williams et al. 2019). Nevertheless, we acknowledge that using weather radar means that we may miss a few meteotsunamis associated with non-precipitating weather features.

We used radar mosaic images across northwest Europe with 5-km grid spacing. This radar mosaic available at 15-minute intervals, covering 69 out of 71 of the accepted tide gauges (Fig. 1). Although outside of the radar boundary, Lerwick (station 67) and List (station 46) were close enough to the boundary to determine atmospheric forcings. Radar data were processed through several steps at the Met Office before download (Met Office 2003; section 3a in Antonescu et al. 2013).

We decided to link a weather feature to an NSLOTT event if precipitation was over the basin at least 6 h before the first detection. If there was no precipitation over water, the NSLOTT was not classified as a meteotsunami, even if the wave height exceeded 0.25 m.

e. Classifying weather systems by their morphology

From radar-derived precipitation, mesoscale characteristics of atmospheric systems were catalogued. We classified the system motion into one of eight cardinal directions. This motion was the overall motion of the system, constituting of mean flow and propagation (e.g., Markowski and Richardson 2011 p. 251). If possible, we classified the type of mesoscale atmospheric system based on radar morphology (Fig. 2).

We grouped mesoscale atmospheric systems into four classifications: isolated cells, quasi-linear systems, non-linear clusters and open-cellular convection (Fig. 2). Isolated cells were discrete, small regions of precipitation, with precipitation rates exceeding 2 mm h^{-1}. Two types of isolated cells were seen. Most isolated cell morphologies were poorly organised cells (Fig. 2a), but there were examples more linearly-organised precipitation with cells that moved parallel to the line orientation (i.e. roll bands). Roll-band systems were classified as isolated cells because of the cross-section of the system relative to its motion. Conversely, quasi-linear systems were more organised convective systems (Fig. 2b). This category included broken lines, non-stratiform lines, stratiform lines, bow echoes, and frontal rain bands (e.g., Gallus et al. 2008; Cotton et al. 2011; Antonescu et al. 2013; Bechle et al. 2016). When cells were more poorly organised but were connected by regions of precipitation exceeding 2 mm h^{-1}, they were classified as non-linear clusters (Fig. 2c). The final classification was open-cellular convection, or open cells (Fig. 2d). Open-cellular convection was connected showery regions with clear centres (e.g., de Jong and Battjes 2004; Cotton et al. 2011). Though not defining features of the mesoscale atmospheric systems and provided here for clarity, open cells often moved southwards, eastwards or south-eastwards (about 90%) and covered large regions (order of 10,000 km^2), whereas isolated cells moved northwards or north-eastwards (about 80%) and were much smaller (order of 100–10,000 km^2) (cf. Fig. 2a(ii) with Fig.2d(ii)).

If there were multiple precipitating weather systems, those that occurred for longer times and were closer to the time and location of meteotsunami detection were favoured for classification.

As there was uncertainty classifying the precipitating system morphologies, a confidence was assigned to each system classification. Classification confidence did not affect meteotsunami identification but if the wave occurred more than 6 h from the system and there were multiple systems in quick succession, or if the final system classification could have been in three or more categories, then the system type was "unclassified". Conversely, "Confidently" classified systems (which we further analyse) all occurred within 3 h of the meteotsunami and were firmly in one classification. Once the mesoscale systems were classified, the concurrent synoptic atmospheric environments for a subset of meteotsunami-generating mesoscale systems were found from ERA5 reanalysis data (Copernicus Climate Change Service 2017).

To summarise, we classify an NSLOTT as a non-tidal wave with a 2–120-min period and a wave height (peak to trough) that is ≥ 6σ of the sea-level residual. The sea-level residual is the sea-level elevation with as much tidal signal suppressed as possible, through both 120-min high-pass filtering and a stacking algorithm. An NSLOTT also had to have its signal identified at ≥ 2 tide gauges within 3 h. Requiring two tide gauges to measure an event to classify as an NSLOTT may result in conservative estimates of meteotsunami recurrence rates (e.g. tide gauges in Ireland and Lerwick). For the purposes of this climatology, a meteotsunami is an NSLOTT that had a minimum calculated 0.25-m wave height (i.e. a high-amplitude NSLOTT) and occurred within 6 h of a precipitating atmospheric system. Atmospheric systems were then classified into one of four system morphologies, and only systems that were confidently classified are presented.

3. Results and discussion

After developing the meteotsunami and atmospheric system classification datasets, this section presents the typical meteotsunami size-exceedance rates (section 3a), when meteotsunamis occurred (section 3b), which mesoscale atmospheric systems were coincident with meteotsunamis (section 3c), and a brief summary of their synoptic setting (section 3d). Towards the end of each section, the results are discussed relative to other regions and how they relate to previous northwest European studies.

a. Size-exceedance rates

Although case studies and localised climatologies suggest that meteotsunamis are typically smaller than 1 m in the UK and the Netherlands, if a large meteotsunami occurs (e.g., > 1 m), there is currently little information of the probability of this occurrence. In this section, the NSLOTT identification rate, meteotsunami identification rate and meteotsunami size-exceedance rates are presented to provide such information.

1) RESULTS

A total of 13 080 initial detections exceeded the 6σ-threshold (Table 2). From these initial detections, 2339 NSLOTTs were identified at two or more tide gauges within 3 h (18% of initial detections). Of these NSLOTTs, 378 had wave heights greater than 0.25 m (16% of NSLOTTs). From these high-amplitude NSLOTTs, 349 (92%) occurred within 6 h of precipitation and were classed as meteotsunamis in this study.

Across the entire study region, an average of 355 NSLOTTs per year and 54.0 meteotsunamis per year were identified (Table 2). France had most identified meteotsunamis per year (15.4), followed by Ireland (13.3), the Netherlands (10.7), Belgium (5.9) and Germany (4.7). The country with the fewest identified meteotsunamis per year was the UK (4.0), despite over half of all NSLOTT identifications. A larger reduction between NSLOTT count and meteotsunami count occurred after the 0.25-m amplitude threshold was applied in the UK than any other country. In contrast, 31% of NSLOTTs were identified in Ireland and France but had 66% of identified meteotsunamis. Therefore, the combined processing of sea-level elevation meant that, overall, NSLOTTs occurred 6.6 times more frequently than meteotsunamis, and locations with the most identified NSLOTTs (UK) did not necessarily have the most identified meteotsunamis (Ireland and France).

Although large (> 1 m) meteotsunamis occurred four times during the study period, most detected meteotsunamis were small. The median meteotsunami wave height was between 0.27–0.40 m between each country, and no meteotsunamis were larger than 1.5 m. Of 349 meteotsunamis, 213 (61%) were larger than 0.3 m and 72 (21%) were larger than 0.5 m. Meteotsunamis larger than 0.5 m were mainly identified in France (51%) and Ireland (36%) and were only detected at 14 out of 71 tide gauges (bold location names in Fig. 1). Of the four meteotsunamis that were larger than 1 m, one was identified at Dunmore East (station 86) and three were identified at Le Havre (station 9).

Countries with smaller data intervals (5–6 min) had lower annual size-exceedance rates for smaller thresholds than countries with larger data intervals (Fig. 3,). In other words, smaller NSLOTTs were detected less often with smaller data intervals (see Appendix F of Williams (2020) for more detail). Wave-height aliasing likely meant that NSLOTTs exceeding 0.1 m were identified more frequently with longer data intervals. This increase in small NSLOTT identifications occurred because aliasing had two effects. First, the 6σ thresholds were lower with longer data intervals than with shorter data intervals, implying that more, smaller NSLOTTs were identified at tide gauges with longer data intervals. Second, because wave heights were aliased, fewer large waves were identified that met the 0.25-m minimum NSLOTT wave height. In locations with shorter data intervals, larger waves were identified as NSLOTTs, even though there were other smaller detections.

Although the UK had smaller meteotsunamis identified than elsewhere (0.27-m median wave height), these meteotsunamis may have been larger but were reduced due to the 15-min averaging interval used. The largest meteotsunamis in the UK were measured at Lowestoft (station 59 in Fig. 1), north Scotland (stations 67–70) and along the south coast (stations 48, 49, 52 and 55). Of these stations, Lerwick (station 67) and the south coast have historically experienced meteotsunamis and seiching (e.g., Sibley et al. 2016; Pugh et al. 2020).

The effect of wave-height aliasing was less obvious in Ireland, with the largest 6σ-thresholds and most NSLOTTs exceeding 0.25 m of all countries. Interestingly, more detections were filtered out here than elsewhere when applying the event interval. Only 14% of 6σ events were identified at two or more tide gauges within 3 h (Table 2). This relatively low conversion rate occurred because there were only five tide gauges that were spread across three different coastlines. For example, although three waves greater than 1-m were detected at Malin Head (station 90), none of these waves were detected at the other Irish tide gauges within this analysis. Therefore, this estimate is likely conservative for the frequency of meteotsunamis in Ireland, because the tide gauges used here are relatively sparse and because we exclude tide gauges on the western coastline. In contrast, 21% of 6σ-events in Belgium passed the event interval (Table 2). This higher conversion rate was probably because the four Belgian stations only spanned 40 km of coastline, all of which bordered the North Sea. Therefore, sparser measurements also reduced the number of detected meteotsunamis.

2) DISCUSSION

Of the identified meteotsunamis, the median and maximum wave heights were similar to those found in the Great Lakes (Bechle et al. 2015; Bechle et al. 2016), the US East Coast (Dusek et al. 2019), the Gulf of Mexico (Olabarrieta et al. 2017) and most of the Mediterranean (Šepić et al. 2015b). These regions have median wave heights of about 0.4 m and waves that rarely exceed 1 m (e.g., Olabarrieta et al. 2017; Dusek et al. 2019). We identified about a tenth as many small meteotsunamis (0.25–0.3 m) as the Great Lakes, but a similar number of large meteotsunamis (0.5–1 m) (Bechle et al. 2016). We probably identified fewer small meteotsunamis because we applied stricter amplitude thresholds and event intervals than applied in the Great Lakes (Table 1). However, a similar number of large meteotsunamis indicates a similar (if not directly comparable) meteotsunami wave-height climate in northwest Europe and the US basins.

Although meteotsunamis in northwest Europe are about the same height as elsewhere, there are only a few reported events of flooding in the media (e.g., 27 June 2011 in the UK, 29 May 2017 in the Netherlands). Meteotsunamis may not be as hazardous in this region as elsewhere because the typical tidal ranges are an order of magnitude larger than the median meteotsunami wave height (Fig. 1). Similarly, small meteotsunamis in relatively large tidal ranges have been reported in British Columbia (Thomson et al. 2009) and across the globe (Vilibić and Šepić 2017). Although meteotsunami wave heights are much smaller than tidal amplitudes, meteotsunami currents may still be dangerous. Overall, meteotsunami-related flooding rarely happens in northwest Europe because meteotsunamis are typically much smaller than the tidal range, although the currents associated with meteotsunamis may still pose a hazard.

Finally, although the reduction of size-exceedance rates may be progressively larger with longer intervals, relative comparisons between countries are possible. In this dataset, we can compare countries with the same interval. More and larger meteotsunamis were detected in France than in Germany and the Netherlands. Furthermore, larger meteotsunamis were identified more frequently France with longer averaging intervals (10 min) than Ireland with shorter averaging intervals (5 and 6 min). Thus, more meteotsunamis probably occurred in France than Ireland. Also, in France (10 min), Ireland (5 and 6 min), the Netherlands (10 min) and Germany (10 min), large meteotsunamis were detected more frequently than in Belgium (5 min), meaning that fewer meteotsunamis probably occurred in Belgium than these other countries. However, how the rate of meteotsunami occurrence in the UK compares to the other countries remains unknown. Because the 15-min averaging interval appears to be too long to properly identify NSLOTT wave heights, more meteotsunamis could have been detected in the UK with shorter averaging intervals.

b. Seasonal and diurnal variation

The seasonal and diurnal variation analyses show when meteotsunamis occur. This information is potentially useful, an example being that meteotsunami identifications can be cross-referenced with times of beach use.

1) RESULTS

Across every country, more meteotsunamis were identified in winter than any other season (Fig. 4). In Ireland and the UK, 58–59% of all meteotsunamis were identified in winter, and 44–46% occurred in December and January. In France, Belgium, the Netherlands, and Germany most meteotsunamis also occurred in winter (43–46% of all meteotsunamis).

Every country apart from the UK had an annual cycle with a single winter peak and the fewest meteotsunamis in either spring or summer (Fig. 4). The season with fewest meteotsunamis was between 0–15% of each country's total meteotsunami count. In contrast, the UK showed an annual cycle with a secondary summer peak. Even though only 32 meteotsunamis were recorded in the UK, summertime meteotsunamis were identified in 5 out of 8 years.

All detections related to high-amplitude NSLOTTs were then grouped by hour (e.g., 1400–1459 UTC) and month (e.g., Jan), allowing analysis of both seasonal and diurnal variation. In total, 1368 detections were analysed. Again, there was strong seasonal variation, with over 52% of detections occurring in winter and only 7% in summer (Fig. 5). A higher winter maximum and lower summer minimum were found by analysing all of the available detections than by grouping the detections as a single event with the largest wave height, because more tide gauges identified a 6σ-event per high-amplitude NSLOTT during winter than summer.

Thus, winter events were detected more frequently and by more tide gauges than summer events.

Throughout the year, there was a weak diurnal cycle, with detections peaking in the afternoon (30%) and falling overnight (23%) (Fig. 5). Most meteotsunamis occurred in winter, primarily in the afternoon, although there was also a secondary winter peak overnight. The diurnal cycle was about 5–6 times weaker than the seasonal cycle and was slightly variable throughout the year. For example, the overnight peak occurred between winter and autumn, but not spring or summer.

2) DISCUSSION

Although most meteotsunamis in northwest Europe occurred in autumn and winter, case studies produced over the past 10 years have focussed on meteotsunamis from eyewitness reports in late spring and summer (Tappin et al. 2013; Frère et al. 2014; Sibley et al. 2016; Thompson et al. 2020). The first known occurrence of a fatal wave in the English Channel that was generated by a squall line also occurred in summer (Douglas 1929). This study suggests that these case studies are not representative of the meteotsunami seasonality in northwest Europe. Other localised climatologies have suggested that winter meteotsunamis are more frequent. In the Netherlands, over half of seiches in Rotterdam occurred in winter, with fewest in late spring and summer (de Jong and Battjes 2004). In the Solent and south coast of the UK, eight of the largest waves with 3–5-h periods were in autumn or winter (Oszoy et al. 2016). Similar seasonality of seiches have been found from a local climatology across Shetland (Pugh et al. 2020). Our results are consistent with the seasonality of these localised climatologies. We reject that meteotsunamis are primarily a summer-time phenomenon in north-west Europe.

We suggest that this discrepancy in the seasonality between case studies and climatologies is not explained because meteotsunamis are larger in summer than winter. In this study, in France the meteotsunamis were on average 0.47 m high in winter and 0.38 m high in summer. Therefore, in combination with the increased frequency and across more stations, meteotsunamis should be noticed more frequently in winter than summer. It may be that identifying a meteotsunami is more difficult in the winter, when there are also larger wind waves (e.g., Woolf et al. 2002; Shi et al. 2019) and storm surges (e.g., Haigh et al. 2010). This difficulty in identification is evident in Thompson et al. (2020), with most meteotsunamis from historical documents identified in the summer, whilst similarly described events in autumn and winter are identified as storm waves, swell waves, or storm surges (e.g. Chesil Beach 1824, Bristol Channel 1910). Nevertheless, this bias could also be attributed to earlier authors primarily studying the observed summer-time meteotsunamis (e.g. Haslett et al. 2009; Tappin et al. 2013; Frère et al. 2014; Sibley et al. 2016; Williams et al. 2019), without wholly considering longer term climatologies of other meteotsunami-like waves across Europe (e.g. de Jong et al. 2003; de Jong and Battjes 2004). Furthermore, eyewitness reports may be biased towards the summer, because there are longer daylight hours and more people in coastal regions to make the observations.

Noticeably, none of the 32 meteotsunamis in the Netherlands were in summer (Fig. 4). A lack of summertime identifications in the Netherlands may have occurred because only three years of data were analysed. Nonetheless, these results are consistent with a 7-year climatology in Rotterdam (de Jong and Battjes 2004); summertime meteotsunamis rarely occur in the Netherlands.

c. Analysis of coincident mesoscale weather systems

Finally, atmospheric conditions at the time of meteotsunami detections were examined to identify atmospheric phenomena that generated meteotsunamis. From 378 high-amplitude NSLOTTs, eight were not classifiable because of missing radar data (2%). Of the remaining

370 high-amplitude NSLOTTs, 349 (94%) occurred within 6 h of precipitation and 21 (6%) did not co-occur with precipitation (Table 2). High-amplitude NSLOTTs without co-occurring precipitation may have been formed by non-precipitating atmospheric phenomena or by non-atmospheric phenomena (e.g., landslides). There was no significant difference between the mean wave heights of NSLOTTS without a coincident precipitating system and NSLOTTS with a coincident precipitating system ($p > 0.09$). There was also no significant difference between meteotsunami wave heights for different mesoscale system classifications ($p > 0.26$).

1) RESULTS

Of the identified precipitating systems, only 254 out of 349 (73%, Table 2) were confidently classified into one of the four precipitation morphologies (Fig. 2). Out of 138 high-amplitude NSLOTTs in Ireland and the UK, only 93 systems were confidently classified, because most systems moved in from near the radar boundary edge. However, confidence was also low in several cases because quasi-linear systems were often followed by open cells, making it difficult to determine which system generated the meteotsunami. Furthermore, confidence was low at Ballycotton (station 84) and Dunmore East (station 85) as some quasi-linear systems were slow-moving, with the predominant motion of precipitation parallel to the line orientation. In these instances, it was unclear whether these generating systems were more similar to non-linear clusters (moving parallel to the line orientation) or quasi-linear systems (moving approximately perpendicular to the line orientation). The proportion of confidently classified systems generally increased southwards and eastwards across northwest Europe (cf. Fig. 1 and Fig. 6c), as these coastlines were farther from the radar boundary.

Most of the confidently classified systems were quasi-linear systems (118, or 46%) or open cells (84, or 33%) (Fig. 6a). Fewer classifications were non-linear clusters (44, or 17%) and isolated cells (10, or 4%). However, the variation within this average shows both seasonal and regional variation. There were strong seasonal patterns of meteotsunamis generated by quasi-linear systems and open cells (Fig. 6b). Both quasi-linear systems and open cells followed an annual cycle with most occurring in winter and fewest in summer, whereas the isolated cells and non-linear clusters had no clear cycle (Fig. 6b).

Regionally, locations with more meteotsunamis tended to have higher counts of every classification, but those with proportionally more wintertime meteotsunamis (e.g., Ireland and the UK) tended to have even more open-cell classifications (Fig. 6c). Non-linear cluster identifications tended to increase with total number of meteotsunamis, remaining between 14–22% for every country apart from the Netherlands (4%). Quasi-linear system classifications also increased with larger totals, with the exception of Ireland, which had fewer quasi-linear classifications than Belgium. However, despite similar seasonal patterns between countries, there was regional variation between open-cell classifications. Open-cell classifications were higher in Ireland, the UK and Germany than France, Belgium and the Netherlands. Across individual countries, if the proportion of open cells was relatively low compared to average (< 33%), the proportion of quasi-linear systems was relatively high (> 46%) and vice versa.

2) DISCUSSION

These results support and extend the mesoscale analysis of de Jong et al. (2003) across northwest Europe, who originally showed that cold fronts, split cold fronts (both of these being classified as quasi-linear systems in this work) and open cells can generate seiching in the Netherlands. From the data provided here, open cells generated about 25% of meteotsunamis (33% of classifications). However, the mechanisms through which open cells generate waves remains uncertain, alongside whether more linear systems preferentially generate meteotsunamis. As a point of comparison, we note that the spiral rainbands from tropical cyclones in the Gulf of Mexico (Shi et al. 2020) and 'linear', 'bow' and 'frontal' systems in the Great Lakes (Bechle et al. 2016) would have been quasi-linear systems under the criteria considered here. Nonetheless, the combined evidence presented here is not sufficient to distinguish whether meteotsunamis are preferentially generated by linear systems rather than circular systems, as proposed by Williams et al. (2020). More generally, data from the 5-km radar with 15-min intervals and tide gauges with 5–15-min intervals were too temporally coarse to identify the specific feature of an atmospheric system that generated a meteotsunami in systems with multiple components.

However, this analysis broadly agrees with those conducted in the Laurentian Great Lakes, which showed that less than 5% of meteotsunamis were generated by isolated cells (Bechle et al. 2015, 2016). This result may be partially explained by inefficient transfer of energy to the ocean by small, circular surface forcings even when moving at Proudman-resonant speeds (Williams et al. 2020). However, fewer meteotsunami may be formed by isolated cells because they also cover a smaller area than other systems and because they may have lower surface pressure gradients and wind stresses.

We suggest that using radar to classify meteotsunamis is about as successful as using *in situ* surface pressure and wind speed measurements. We linked 92% of NSLOTTs exceeding 0.25 m to weather systems using the radar method. Comparably, in the Great Lakes, fewer NSLOTTs were classified as meteotsunamis by linking waves with pressure and wind fluctuations measured at coastlines (87%) (Bechle et al. 2016). This comparably high identification rate provides support for our radar-only method for northwest Europe. Radar classification may also be useful information for future operational meteotsunami forecasting (e.g. Bechle et al. 2016). Quantifying the specificity (true negative rate) and sensitivity (true positive rate) of such an approach could be achieved by cross-examining mesoscale precipitating features with meteotsunami occurrences over a given period.

d. Analysis of coincident synoptic-scale weather systems

Next, we present a brief summary of the synoptic composite atmospheric analyses associated with this climatology. Synoptic-scale composite analyses allow understanding of the average thermodynamic and kinematic weather patterns associated with meteotsunamis (e.g., Šepić et al. 2015b; Vilibić and Šepić 2017). We used ERA5 Reanalysis output, which is common in other meteotsunami studies that focus on coincident synoptic patterns (e.g., Belušić et al. 2007; Tanaka 2010; Denamiel et al. 2019; Shi et al. 2019).

Here, we focus on the synoptic composite analyses for meteorological conditions favourable for meteotsunamis that affected the French coastline. Most of these tide gauges border the English Channel, except for Dunkirk, which borders the North Sea (station 13). The synoptic composite analysis included 10 events with wintertime open cells, 26 events with wintertime quasi-linear systems and 9 events with summertime quasi-linear systems. We examined sea-level pressure, 500-hPa geopotential height, the temperature difference between 850 hPa and the sea surface (ΔT_{SS}), and convective available potential energy (CAPE) (Fig. 7).

All synoptic environments indicated that the dominant synoptic weather feature at the time of meteotsunami detection were extratropical cyclones north or west of the UK (Fig. 7). Although sea-level low-pressure centers were associated with all meteotsunamis and favoured westerly geostrophic flow, the associated extratropical cyclones were farther north and about 20 hPa deeper in winter than in summer (Figs. 7ai, 7bi and 7ci). The mean lower- and middle-tropospheric winds were also supportive of eastward-moving mesoscale precipitation systems. We also infer lower tropospheric static instability with open cells and winter quasi-linear systems, as indicated by warmer surface waters compared to lower-tropospheric air (i.e. ΔT_{SS} < -13°C, Figs. 7bi and 7bii) (e.g., Holroyd 1971). Moderate CAPE over ocean occurred for the winter meteotsunamis (Figs. 7ci and 7cii), whereas stronger CAPE over land occurred for the summer meteotsunamis (Fig. 7ciii).

These results agree with previously documented synoptic environments and can help explain the seasonality of each mesoscale system. For example, open cells tend to occur in winter with cold lower-tropospheric air moving over relatively warmer water (e.g., Agee and Dowell 1973; Bakan and Schwarz 1992; de Jong et al. 2003; Vincent et al. 2012). The weaker seasonal variation of meteotsunamis generated by quasi-linear systems was because the quasi-linear system classification included a wide range of systems that occurred throughout the year. For example, narrow cold-frontal rainbands may occur with extratropical cyclones in winter (e.g., Fig. 2b, Fairman et al. 2017) and quasi-linear mesoscale convective systems (MCS) may occur in summer. The quasi-linear summertime synoptic composite presented here has high CAPE over continental Europe and is broadly consistent with a Spanish Plume pattern (Fig. 7ciii, Carlson and Ludlam 1968; Morris 1986; Lewis and Gray 2010). Interestingly, the sea-level pressure fields, air temperatures and environmental flow patterns presented here are similar to those observed for other seiches (3–5 h periods) in the English Channel (Oszoy et al. 2016).

External resonance may also be inferred from reanalysis fields. By using the tropospheric wind speed at a specified level that represents the translation speeds of mesoscale phenomena (700 hPa), external resonance may be inferred where the tropospheric wind speed and shallow-water wave speed match within a predefined threshold (here 20%) (e.g., Šepić et al. 2016). Using this criterion, meteotsunamis were formed with Proudman-resonant regions across the English Channel in 43 out of 45 instances (not shown). These Proudman-resonant regions were common between mesoscale systems, despite synoptic sea-level pressure centers with different magnitudes and locations.

4. Conclusions

This study has produced a regional climatology of meteotsunamis across northwest Europe. Through a combination of manual filtering, automatic peak detection and a stacking algorithm designed to remove tidal signals, 13 080 events greater than a 6σ-threshold were identified across 71 tide gauges between 2010–2017. From these events, 2339 NSLOTTs were identified (occurring at two or more stations within 3 h) and 349 meteotsunamis were identified (high-amplitude NSLOTTs occurring within 6 h of a precipitating system), yielding 355 NSLOTTs per year or 54.0 meteotsunamis per year. From this meteotsunami dataset, the typical sizes and times of 349 meteotsunamis were extracted, the morphology of 256 mesoscale atmospheric systems that generated meteotsunamis were classified and 45 synoptic atmospheric composites were determined for a subset of meteotsunamis in France.

Although tide-gauge data intervals were large (5–15 min) compared to the typical period of meteotsunamis (2–120 min), median wave heights were between 0.27–0.40 m for each country. The largest meteotsunamis in northwest Europe occurred most frequently in France and the Republic of Ireland. From all meteotsunamis, the three largest meteotsunamis (~ 1 m) were measured in Le Havre (10-min intervals). Most meteotsunamis were small, with 79% smaller than 0.5-m high.

We recognise that relatively long intervals in tide gauges were used to study meteotsunamis compared to elsewhere. We suggest that, the 15-min data interval in the UK is too long to provide a representative meteotsunami wave-height climatology. However, this analysis does not answer what would be a sufficiently small interval. It is highly likely that smaller intervals would increase meteotsunami size-exceedance rates. It is also strongly recommended in future climatologies that smaller intervals from tide gauges are analysed. For example, 5–6-minute averaging intervals are recommended for studying tsunamis as part of the Global Sea-Level Observing System (IOC 2006). Nonetheless, considering the manual processing challenges faced here, 1-min data may need automated methods with rigorously removed tidal signals.

Despite the large intervals used, we expect that the seasonal cycle extracted is valid, as there is no reason to expect seasonal bias in aliasing from tide-gauge measurements. Furthermore, all seasonal analyses from tide gauges tended to agree. In Ireland, France, Belgium, the Netherlands and Germany, there was a single annual cycle, with most meteotsunamis in winter (42–59%) and fewest in spring or summer (0–15%). There was also a diurnal cycle, with most between 1200–1859 UTC (30%) and fewest between 0000–0659 UTC (23%).

To understand which mesoscale weather phenomena were associated with the meteotsunamis, the northwest European radar mosaic with derived precipitation was used to identify and classify mesoscale weather systems occurring within 6 h of each meteotsunami. A mesoscale precipitating feature was identified in 349 out of 378 (92%) large NSLOTT events. This fraction of events identified to occur with a coincident precipitating atmospheric phenomenon is slightly higher than using in situ surface pressure and 10-m wind speeds across the Great Lakes (87%). We suggest that this relatively high conversion rate shows the value in our radar-only method of atmospheric generation for meteotsunamis in northwest Europe. To our knowledge, this radar-only method has not been considered before. From the 256 classified precipitating mesoscale phenomena, most were quasi-linear systems (46%) or open cells (33%), with some non-linear clusters (17%) and very few isolated cells (4%) (Figs. 2 and 6). Most quasi-linear systems and open cells occurred in the winter and fewest occurred in summer, whereas non-linear clusters and isolated cells had no clear seasonal cycle. Open-cell classifications were dominant in Ireland and the UK, whereas quasi-linear systems were dominant along the French, Belgian, Dutch and German coastlines.

To further explain the conditions where mesoscale atmospheric phenomena formed, we analyzed the synoptic atmospheric composites using output from the ERA5 reanalysis. These synoptic composites were focussed on the French coastline, with data between 2010–2017 from seven tide gauges bordering the English Channel and one tide gauge bordering the North Sea.

The synoptic conditions here are typical of those that produce wintertime open cells, wintertime quasi-linear systems and summertime quasi-linear systems. Notably, 43 out of 45 analysed meteotsunamis from the French coast of the English Channel were coincident with a region that the ratio between the 700-hPa wind speed and shallow-water wave speed without tides was between 0.8–1.2. From this result, we infer that Proudman resonance is a plausible explanation for most of the meteotsunamis along the French coastline, and possibly across northwest Europe.

To conclude, we detected 349 meteotsunamis, with an average rate of 54.0 per year, which is similar to the Great Lakes, Gulf of Mexico, US East Coast, and parts of the Mediterranean. However, at least four factors identified in this study may combine to explain why meteotsunamis are not considered common in northwest Europe, at least from eye-witness accounts. The detected meteotsunamis in northwest Europe were frequently small (only 21% of meteotsunamis were larger than 0.5 m), occurred in basins with tides an order of magnitude larger than their wave height (0.27–0.4 m median wave height compared to 3–8 m tidal range), occurred mostly in winter (48–52%), and occurred within 6 h of precipitating systems (92%).

Acknowledgements David Williams was funded by the National Environmental Research Council's Understanding the Earth, Atmosphere and Ocean Doctoral Training Programme, Grant NE/L002469/1.

Data availability statement Atmospheric datasets were accessed from the Centre for Environmental Data Analysis (which collated data from Met Éireann, the Met Office, Météo France, the Royal Meteorological Institute of Belgium, the Royal Netherlands Meteorological Institute and Deutscher Wetterdienst). Oceanographic tide gauge datasets were accessed from

the Marine Institute, the British Oceanographic Data Centre, and the Copernicus Marine Environment Monitoring Service (which collated data from the Naval Hydrographic and Oceanographic Service, the Belgian Marine Data Centre, the National Oceanographic Data Centre for the Netherlands and the German Oceanographic Data Centre).

References

Agee, E.M., and K.E. Dowell, 1974: Observational Studies of Mesoscale Cellular Convection. *J. Appl. Meteorol.*, **13**, 46–53, doi:10.1175/1520-0450(1974)013<0046:OSOMCC>2.0.CO;2.

Anderson, E.J., A.J. Bechle, C.H. Wu, D.J. Schwab, G.E. Mann, and K.A. Lombardy, 2015: Reconstruction of a meteotsunami in Lake Erie on 27 May 2012: Roles of atmospheric conditions on hydrodynamic response in enclosed basins. *J. Geophys. Res. Oceans*, **120**, 8020–8038, doi:10.1002/2015JC010883.

Antonescu, B., G. Vaughan, and D.M. Schultz, 2013: A Five-Year Radar-Based Climatology of Tropopause Folds and Deep Convection over Wales, United Kingdom. *Mon. Weather Rev.*, **141**, 1693–1707, doi:10.1175/MWR-D-12-00246.1.

Bakan, S., and E. Schwarz, 1992: Cellular convection over the North-Eastern Atlantic. *Int. J. Climatol.*, **12**, 353–367, doi:10.1002/joc.3370120404.

Bechle, A.J., D.A.R. Kristovich, and C.H. Wu, 2015: Meteotsunami occurrences and causes in Lake Michigan. *J. Geophys. Res. Oceans*, **120**, 8422–8438, doi:10.1002/2015JC011317.

Bechle, A.J., C.H. Wu, D.A.R. Kristovich, E.J. Anderson, D.J. Schwab, and A.B. Rabinovich, 2016: Meteotsunamis in the Laurentian Great Lakes. *Sci. Rep.*, **6**, 37832, doi:10.1038/srep37832.

Belušić, D., B. Grisogono, and Z.B. Klaić, 2007: Atmospheric origin of the devastating coupled air-sea event in the east Adriatic. *J. Geophys. Res. Atmos.*, **112**, D17111, doi:10.1029/2006JD008204.

Butterworth, S., 1930: On the Theory of Filter Amplifiers. *Exp. Wireless Wireless Eng.*, **7**, 536–541.

Carlson, T.N., and F.H. Ludlam, 1968: Conditions for the occurrence of severe local storms. *Tellus*, **20**, 203–226, doi:10.1111/j.2153-3490.1968.tb00364.x.

Carvajal, M., M. Contreras-López, P. Winckler, and I. Sepúlveda, 2017: Meteotsunamis occurring along the southwest coast of South America during an intense storm. *Pure Appl. Geophys.*, **174**, 3313–3323, doi:10.1007/s00024-017-1584-0.

Choi, B.J., C. Hwang, and S.H. Lee, 2014: Meteotsunami-tide interactions and high-frequency sea level oscillations in the eastern Yellow Sea. *J. Geophys. Res. Oceans*, **119**, 6725–6742, doi:10.1002/2013JC009788.

Copernicus Climate Change Service (C3S), 2017: *ERA5: Fifth generation of ECMWF atmospheric reanalyses of the global climate*. Copernicus Climate Change Service Climate Data Store (CDS), 26 July 2019, https://cds.climate.copernicus.eu/cdsapp#!/home.

Cotton, W.R., G.H. Bryan, and S.C. van den Heever, 2011: *Storm and Cloud Dynamics*. Second Edition, Academic Press, 809 pp.

de Jong, M.P.C., and J.A. Battjes, 2004: Low-frequency sea waves generated by atmospheric convection cells. *J. Geophys. Res. Oceans*, **109**, C01011, doi:10.1029/2003JC001931.

de Jong, M.P.C., L.H. Holthuijsen, and J.A. Battjes, 2003: Generation of seiches by cold fronts over the southern North Sea. *J. Geophys. Res. Oceans*, **108**, 3117, doi:10.1029/2002JC001422.

Denamiel, C., J. Šepić, D. Ivanković, and I. Vilibić, 2019: The Adriatic Sea and Coast modelling suite: Evaluation of the meteotsunami forecast component. *Ocean Modell.*, **135**, 71–93, doi:10.1016/j.ocemod.2019.02.003.

Douglas, C.K.M., 1929: The line-squall and channel wave of July 20th, 1929. *Meteorol. Mag.*, **64**, 187–189.

Dusek, G., C. DiVeglio, L. Licate, L. Heilman, K. Kirk, C. Paternostro, and A. Miller, 2019: A Meteotsunami Climatology along the U.S. East Coast. *Bull. Amer. Meteor. Soc.*, **100**, 1329–1345, doi:10.1175/BAMS-D-18-0206.1.

Dziewoński, A.M., T.A. Chou, and J.H. Woodhouse, 1981: Determination of Earthquake Source Parameters From Waveform Data for Studies of Global and Regional Seismicity. *J. Geophys. Res. Solid Earth*, **86**, 2825–2852, doi:10.1029/JB086iB04p02825.

Ekström, G., M. Nettles, and A.M. Dziewoński, 2012: The global CMT project 2004–2010: Centroid-moment tensors for 13,017 earthquakes. *Phys. Earth Planet. Inter.*, **200–201**, 1–9, doi:10.1016/j.pepi.2012.04.002.

Fairman, J.G. Jr., D.M. Schultz, D.J. Kirshbaum, S.L. Gray, and A.I. Barrett, 2017: Climatology of Size, Shape, and Intensity of Precipitation Features over Great Britain and Ireland. *J. Hydrometeorol.*, **18**, 1595–1615, doi:10.1175/JHM-D-16-0222.1.

Frère, A., C. Daubord, A. Gailler, and H. Hébert, 2014: Sea level surges of June 2011 in the NE Atlantic Ocean: observations and possible interpretation. *Nat. Hazards*, **74**, 179–196, doi:10.1007/s11069-014-1103-x.

Gallus, W.A. Jr., N.A. Snook, and E.V. Johnson, 2008: Spring and Summer Severe Weather Reports over the Midwest as a Function of Convective Mode: A Preliminary Study. *Weather Forecast.*, **23**, 101–113, doi:10.1175/2007WAF2006120.1.

Greenspan, H.P., 1956: The generation of edge waves by moving pressure distributions. *J. Fluid Mech.*, **1**, 574–592, doi:10.1017/S002211205600038X.

Haigh, I.D., M.P. Wadey, T. Wahl, O. Ozsoy, R.J. Nicholls, J.M. Brown, K.J. Horsburgh, and B. Gouldby, 2016: Spatial and temporal analysis of extreme sea level and storm surge events around the coastline of the UK. *Sci. Data*, **3**, 160107, doi:10.1038/sdata.2016.107.

Haslett, S.K., H.E. Mellor, and E.A. Bryant, 2009: Meteo-tsunami hazard associated with summer thunderstorms in the United Kingdom. *Phys. Chem. Earth.*, **34**, 1016–1022, doi:10.1016/j.pce.2009.10.005.

Hibiya, T., and K. Kajiura, 1982: Origin of the Abiki Phenomenon (a Kind of Seiche) in Nagasaki Bay. *J. Oceanogr. Soc. Japan*, **38**, 172–182, doi:10.1007/BF02110288.

Holroyd, E.W. III, 1971: Lake-effect cloud bands as seen from weather satellites. *J. Atmos. Sci.*, **28**, 1165–1170, doi:10.1175/1520-0469(1971)028<1165:LECBAS>2.0.CO;2.

IOC, 2006: *Manual on sea level measurement and interpretation.* Volume IV-An update to 2006. Intergovernmental Oceanographic Commission, Manuals and Guides, 14, Paris.

Johnson, R.H., 2001: Surface Mesohighs and Mesolows. *Bull. Amer. Meteor. Soc.*, **82**, 13–32, doi:10.1175/1520-0477(2001)082<0013:SMAM>2.3.CO;2.

Kim, H., M.S. Kim, H.J. Lee, S.B. Woo, and Y.K. Kim, 2016: Seasonal Characteristics and Mechanisms of Meteo-tsunamis on the West Coast of Korean Peninsula. *J. Coast. Res.*, **75**, 1147–1151, doi:10.2112/SI75-230.1.

Lewis, M.W., and S.L. Gray, 2010: Categorisation of synoptic environments associated with mesoscale convective systems over the UK. *Atmos. Res.*, **97**, 194–213, doi:10.1016/j.atmosres.2010.04.001.

Ličer, M., B. Mourre, C. Troupin, A. Krietemeyer, A. Jansá, and J. Tintoré, 2017: Numerical study of the Balearic meteotsunami generation and propagation under synthetic gravity wave forcing. *Ocean Modell.*, **111**, 38–45, doi:10.1016/j.ocemod.2017.02.001.

Linares, Á., C.H. Wu, A.J. Bechle, E.J. Anderson, and D.A.R. Kristovich, 2019: Unexpected rip currents induced by a meteotsunami. *Sci. Rep.*, **9**, 2105, doi:10.1038/s41598-019-38716-2.

Linares, Á., A.J. Bechle, and C.H. Wu, 2016: Characterization and assessment of the meteotsunami hazard in northern Lake Michigan. *J. Geophys. Res. Oceans*, **121**, 7141–7158, doi:10.1002/2016JC011979.

Markowski, P., and Y. Richardson, 2011: *Mesoscale Meteorology in Midlatitudes*. Vol. 2. John Wiley & Sons, 430 pp.

Met Office, 2003: *Met Office rain radar data from the NIMROD system*. NCAS British Atmospheric Data Centre, http://catalogue.ceda.ac.uk/uuid/82adec1f896af6169112d09cc1174499.

Morris, R.M., 1986: The Spanish Plume – Testing the Forecasters Nerve. *Meteorol. Mag.*, **115**, 349–357.

Monserrat, S., I. Vilibić, and A.B. Rabinovich, 2006: Meteotsunamis: Atmospherically induced destructive ocean waves in the tsunami frequency band. *Nat. Hazards Earth Syst. Sci.*, **6**, 1035–1051, doi:10.5194/nhess-6-1035-2006.

Olabarrieta, M., A. Valle-Levinson, C.J. Martinez, C. Pattiaratchi, and L. Shi, 2017: Meteotsunamis in the northeastern Gulf of Mexico and their possible link to El Niño Southern Oscillation. *Nat. Hazards*, **88**, 1325–1346, doi:10.1007/s11069-017-2922-3.

Orlić, M., 1980: About a possible occurrence of the Proudman resonance in the Adriatic. *Thalassia Jugoslavica*, **16**, 79–88.

Orlić, M., D. Belušić, I. Janeković, and M. Pasarić, 2010: Fresh evidence relating the great Adriatic surge of 21 June 1978 to mesoscale atmospheric forcing. *J. Geophys. Res. Oceans*, **115**, C06011, doi:10.1029/2009JC005777.

Oszoy, O., I.D. Haigh, M.P. Wadey, R.J. Nicholls, and N.C. Wells, 2016: High-frequency sea level variations and implications for coastal flooding: A case study of the Solent, United Kingdom. *Cont. Shelf Res.*, **122**, 1–13, doi:10.1016/j.csr.2016.03.021.

Pattiaratchi, C., and E.M.S. Wijeratne, 2014: Observations of meteorological tsunamis along the south-west Australian coast. *Nat. Hazards*, **74**, 281–303, doi:10.1007/s11069-014-1263-8.

Pattiaratchi, C.B., and E.M.S. Wijeratne, 2015: Are meteotsunamis an underrated hazard? *Phil. Trans. R. Soc. A*, **373**, 20140377, doi:10.1098/rsta.2014.0377.

Proudman, J., 1929: The Effects on the Sea of Changes in Atmospheric Pressure. *Geophys. J. Int.*, **2**, 197–209, doi:10.1111/j.1365-246X.1929.tb05408.x.

Pugh, D.T., P.L. Woodworth, and E.M.S. Wijeratne, 2020: Seiches around the Shetland Islands, *Pure Appl. Geophys.*, **177**, 591–620. doi:10.1007/s00024-019-02407-w.

Rabinovich, A.B., 2009: Seiches and Harbor Oscillations. *Handbook of Coastal and Ocean Engineering*, World Sci., Singapore, pp. 193–236, doi:10.1142/9789812819307_0009.

Šepić, J., I. Vilibić, A. Lafon, L. Macheboeuf, and Z. Ivanović, 2015b: High-frequency sea level oscillations in the Mediterranean and their connection to synoptic patterns. *Prog. Oceanogr.*, **137**, 284–298, doi:10.1016/j.pocean.2015.07.005.

Šepić, J., I. Vilibić, and I. Fine, 2015a: Northern Adriatic meteorological tsunamis: Assessment of their potential through ocean modelling experiments. *J. Geophys. Res. Oceans*, **120**, 2993–3010, doi:10.1002/2015JC010795.

Šepić, J., I. Vilibić, and S. Monserrat, 2009: Teleconnections between the Adriatic and the Balearic meteotsunamis. *Phys. Chem. Earth.*, **34**, 928–937, doi:10.1016/j.pce.2009.08.007.

Šepić, J., I. Vilibić, N.S. Mahović, 2012: Northern Adriatic meteorological tsunamis: Observations, link to the atmosphere, and predictability. *J. Geophys. Res. Oceans*, **117**, C02002, doi:10.1029/2011JC007608.

Šepić, J., I. Vilibić, and S. Monserrat, 2016: Quantifying the probability of meteotsunami occurrence from synoptic atmospheric patterns. *Geophys. Res. Lett.*, **43**, 10377–10384, doi:10.1002/2016GL070754.

Shi, L., M. Olabarrieta, A. Valle-Levinson, and J.C. Warner, 2019: Relevance of wind stress and wave-dependent ocean surface roughness on the generation of winter meteotsunamis in the Northern Gulf of Mexico. *Ocean Modell.*, **140**, 101408, doi:10.1016/j.ocemod.2019.101408.

Shi, L., M. Olabarrieta, D.S. Nolan, J.C. Warner, 2020: Tropical cyclone rainbands can trigger meteotsunamis. *Nat. Commun.*, **11**, 678. doi:10.1038/s41467-020-14423-9.

Sibley, A., D. Cox, D. Long, D. Tappin, and K. Horsburgh, 2016: Meteorologically generated tsunami-like waves in the North Sea on 1/2 July 2015 and 28 May 2008. *Weather*, **71**, 68–74, doi:10.1002/wea.2696.

Tanaka, K., 2010: Atmospheric pressure-wave bands around a cold front resulted in a meteotsunami in the East China Sea in February 2009. *Nat. Hazards Earth Syst. Sci.*, **10**, 2599–2610, doi:10.5194/nhess-10-2599-2010.

Tappin, D.R., A. Sibley, K. Horsburgh, C. Daubord, D. Cox, and D. Long, 2013: The English Channel 'tsunami' of 27 June 2011 – a probable meteorological source. *Weather*, **68**, 144–152, doi:10.1002/wea.2061.

Thompson, J., E. Renzi, A. Sibley, and D.R. Tappin, 2020: UK meteotsunamis: a revision and update on events and their frequency. *Weather*.

Thomson, R.E., A.B. Rabinovich, I.V. Fine, D.C. Sinnott, A. McCarthy, N.A.S. Sutherland, and L.K. Neil, 2009: Meteorological tsunamis on the coasts of British Columbia and Washington. *Phys. Chem. Earth.*, **34**, 971–988, doi:10.1016/j.pce.2009.10.003.

Vilibić, I., 2008: Numerical simulations of the Proudman resonance. *Cont. Shelf Res.*, **28**, 574–581, doi:10.1016/j.csr.2007.11.005.

Vilibić, I., and J. Šepić, 2017: Global mapping of nonseismic sea level oscillations at tsunami timescales. *Sci. Rep.*, **7**, 40818, doi:10.1038/srep40818.

Vincent, C.L., A.N. Hahmann, and M.C. Kelly, 2012: Idealized Mesoscale Model Simulations of Open Cellular Convection Over the Sea. *Bound.-Lay. Meteorol.*, **142**, 103–121, doi:10.1007/s10546-011-9664-7.

Vučetić, T., I. Vilibić, S. Tinti, and A. Maramai, 2009: The Great Adriatic flood of 21 June 1978 revisited: An overview of the reports. *Phys. Chem. Earth.*, **34**, 894–903, doi:10.1016/j.pce.2009.08.005.

Wertman, C.A., R.M. Yablonsky, Y. Shen, J. Merrill, C.R. Kincaid, and R.A. Pockalny, 2014: Mesoscale convective system surface pressure anomalies responsible for meteotsunamis along the U.S. East Coast on June 13th, 2013. *Sci. Rep.*, **4**, 7143, doi:10.1038/srep07143.

Williams, D.A., K.J. Horsburgh, D.M. Schultz, and C.W. Hughes, 2019: Examination of Generation Mechanisms for an English Channel Meteotsunami: Combining Observations and Modeling. *J. Phys. Oceanogr.*, **49**, 103–120, doi:10.1175/JPO-D-18-0161.1.

Williams, D.A., K.J. Horsburgh, D.M. Schultz, and C.W. Hughes, 2020: Proudman resonance with tides, bathymetry and variable atmospheric forcings. *Nat. Hazards*. doi: 10.1007/s11069-020-03896-y.

Williams, D.A., 2020: Meteotsunami generation, amplification and occurrence in north-west Europe. Dissertation/thesis, University of Liverpool, 243, doi:10.17638/03073478.

Woolf, D.K., P.G. Challenor, and P.D. Cotton, 2002: Variability and predictability of the North Atlantic wave climate. *J. Geophys. Res. Oceans*, **107**, 3145, doi:10.1029/2001JC001124.

Table 1 Choices made when producing meteotsunami climatological studies.

Study	Study type	Region	Study period	Tide gauge sampling interval	Tide gauges	Isolating wave periods	Amplitude thresholds	Tide gauges and event interval	Atmospheric system data	Number of waves and annual rate
de Jong and Battjes (2004)	Climatology and case studies	North Sea (Rotterdam)	1995–2001	1 min	7	Morlet wavelet analysis	Absolute (0.25 m)	Unknown	In situ	39 (5.6 per year)
Šepić et al. (2012)	Climatology and case studies	Mediterranean	1955–2010	Continuous, digitised to 2 min	1	Filter + Morlet wavelet analysis	Absolute (0.25 m)	Unknown	In situ	14 (and 2 with 140–150 min period)
Pattiaratchi and Wijeratne (2014)	Climatology and case studies	Australia	2000–2013	1–5 min	8	THA + filter	Relative	Unknown	In situ	Unknown
Šepić et al. (2015b)	Climatology and case studies	Mediterranean	2010–2014	1 min	29	THA + filter	Unknown	Recorded by at least 3 tide gauges.	Reanalysis	36 (7.2 per year)
Bechle et al. (2016)	Climatology	Laurentian Great Lakes	1994–2015	6 min	32	Filter	Absolute (0.3 m)	Grouped detections in 12-h intervals.	In situ + Radar	2332 across all lakes (106 per year)
Oszoy et al. (2016)	Case studies found from climatology	English Channel (Solent)	2000–2013	15 min	24	THA + filter.	Relative (Highest energy).	3 days between events.	In situ + reanalysis	Unknown (8 further analyzed, 3–5 period waves)
Kim et al. (2016)	Climatology only	Korea	2002-2013	1 min	9	Filter	Relative (Highest amplitudes).	Recorded by at least 3 tide gauges.	Synoptic charts, radar, lightning, satellite.	92 (7.7 per year)
Vilibić and Šepić (2017)	Climatology only	Global	2004–2017	1 min	366	Filter	Relative (Highest amplitudes).	Unknown	Reanalysis	Unknown (15 further analyzed)
Olabarrieta et al. (2017)	Climatology and case studies	Gulf of Mexico	1996–2016	6 min	3	Filter	Relative (6σ)	36 h imposed between waves.	In situ + Radar	18–25 per year per station
Dusek et al. (2019)	Climatology and case studies	US East Coast	1996–2017	1–6 min	125	THA + filter	Relative and absolute (0.20 m)	Recorded by at least 2 tide gauges.	In situ + Radar	548 (25 per year)

Table 2 Results of NSLOTT identifications grouped across countries, with the study period, number of tide gauges analysed and the interval of those tide gauges. Percentages refer to the number of NSLOTTs that have passed through the thresholds to the total number of NSLOTTs measured at individual stations. IE – Republic of Ireland, UK – United Kingdom, FR – France, BE – Belgium, ND – The Netherlands, DE – Germany

Location	IE	UK	FR	BE	ND	DE	Sum
Study period	2010–2017	2010–2017	2010–2017	2010–2016	2015–2017	2015–2017	n/a
Tide gauges	5	32	8	4	13	9	71
Data interval/ min	5–6	15	10	5	10	10	5–15
Events ≥ 6σ (total)	1401	6602	2589	814	847	782	13,080
6σ-events at two or more tide gauges within 3 h (NSLOTTs)	196 (14%)	1219 (18%)	471 (18%)	170 (21%)	158 (19%)	125 (16%)	2339 (18%)
NSLOTTs per year	24.5	153	58.9	24.3	52.7	41.7	355
NSLOTTs exceeding 0.25 m (total)	116 (8.3%)	32 (0.5%)	140 (5.4%)	42 (5.2%)	33 (3.9%)	15 (1.9%)	378 (2.9%)
High-amplitude NSLOTTs with precipitation within 6 h (Meteotsunamis)	106 (7.6%)	32 (0.5%)	124 (4.8%)	41 (5.0%)	32 (3.8%)	14 (1.8%)	349 (2.7%)
Meteotsunamis per year	13.3	4.0	15.4	5.9	10.7	4.7	54.0

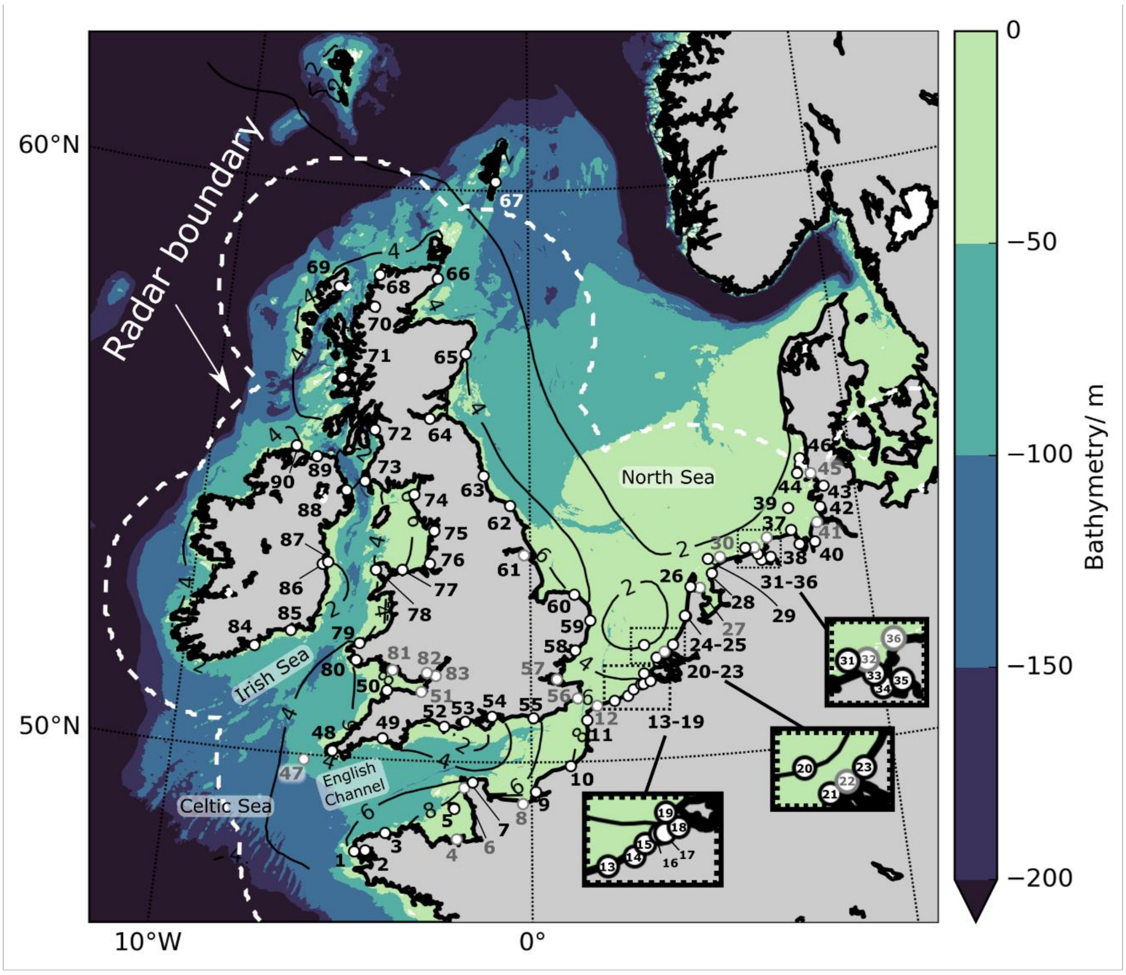

1. **Le Conquet (FR, 10)**
2. Brest (FR, 10)
3. Roscoff (FR, 10)
4. Saint Malo (FR, 10)
5. Jersey (UK, 15)
6. Dielette (FR, 10)
7. Cherbourg (FR, 10)
8. Ouistreham (FR, 10)
9. **Le Havre (FR, 10)**
10. **Dieppe (FR, 10)**
11. **Boulogne (FR,10)**
12. Calais (FR, 10)
13. **Dunkirk (FR, 10)**
14. Nieuwpoort (BE, 5)
15. **Ostend (BE, 5)**
16. **Blankenberge (BE, 5)**
17. Zeebrugge (BE, 5)
18. Cadzand (NL, 10)
19. Vlakte vd Raan (NL, 10)
20. Europlatform (NL, 10)
21. **Brouwershaven (NL, 10)**
22. Haringvliet (NL, 10)
23. Hoek van Holland (NL, 10)
24. IJmondstroompaal (NL, 10)
25. **IJmuiden (NL, 10)**
26. Den Helder (NL, 10)
27. Den Oever(buiten) (NL, 10)
28. Harlingen (NL, 10)
29. Terschelling (NL, 10)
30. Ballum (NL, 10)
31. Huibertgat (NL, 10)
32. Borkum (NL, 10)
33. Eemshaven (NL, 10)
34. Delfzijl (NL, 10)
35. Emden (DE, 10)
36. Norderney (DE, 10)
37. Wangerooge (DE, 10)
38. Willhelmshaven (DE, 10)
39. Helgoland (DE, 10)
40. Bremerhaven (DE, 10)
41. Cuxhaven (DE, 10)
42. Büsum (DE, 10)
43. **Husum (DE, 10)**
44. Hörnum (DE, 10)
45. Dagebüll (DE, 10)
46. List (DE, 10)
47. St. Mary's (UK, 15)
48. Newlyn (UK, 15)
49. Devonport (UK, 15)
50. Ilfracombe (UK, 15)
51. Hinkley Point (UK, 15)
52. Weymouth (UK, 15)
53. Bournemouth (UK, 15)
54. Portsmouth (UK, 15)
55. Newhaven (UK, 15)
56. Dover (UK, 15)
57. Sheerness (UK, 15)
58. Harwich (UK, 15)
59. Lowestoft (UK, 15)
60. Cromer (UK, 15)
61. Immingham (UK, 15)
62. Whitby Bay (UK, 15)
63. North Shields (UK, 15)
64. Leith (UK, 15)
65. Aberdeen (UK, 15)
66. Wick (UK, 15)
67. Lerwick (UK, 15)
68. **Kinlochbervie (UK, 15)**
69. Stornoway (UK, 15)
70. Ullapool (UK, 15)
71. Tobermory (UK, 15)
72. Millport (UK, 15)
73. Portpatrick (UK, 15)
74. Workington (UK, 15)
75. Heysham (UK, 15)
76. Liverpool (UK, 15)
77. Llandudno (UK, 15)
78. Holyhead (UK, 15)
79. Fishguard (UK, 15)
80. Milford Haven (UK, 15)
81. Mumbles (UK, 15)
82. Newport (UK, 15)
83. Avonmouth (UK, 15)
84. **Ballycotton (IE, 6)**
85. **Dunmore East (IE, 6)**
86. Dublin (IE, 5)
87. Howth Harbour (IE, 6)
88. Bangor (UK, 15)
89. Portrush (UK, 15)
90. **Malin Head (IE, 6)**

Figure 1 The study region GEBCO 2014 bathymetry in blue, filled contours from 0 m (light green) to 200 m (dark blue) below mean sea level. Shading saturates beyond 200 m below mean sea level. Tide gauges are shown as white dots, with corresponding numbers indicating locations in the tide-gauge list. Only the tide gauges that were considered are shown. Black outlines and black lettering indicate that the tide gauge was used in further analysis, grey outlines and grey lettering indicate that the tide gauge was discounted. Bold names in the tide gauge list indicate tide gauges that measured a meteotsunami greater than 0.5 m. Two-letter country abbreviations and averaging interval (minutes) are included in brackets (IE – Republic of Ireland, UK – United Kingdom, FR – France, BE – Belgium, ND – The Netherlands, DE – Germany). Tide gauges 13–19, 20–23 and 31–36 are expanded for clarity in the bottom-right hand corner. Indicative tidal ranges were extracted from the POLCOMS North-East Atlantic model between 1–30 Sep 2008 and are shown as thin black lines, with ranges shown every 2 m with thin, black lettering. The boundary of the European radar mosaic is shown as a white dashed line and is defined by the distance 200 km from the nearest radar in the radar networks owned by the meteorological services of the Republic of Ireland (Met Éireann), the UK (Met Office), France (MétéoFrance), Belgium (RMI), the Netherlands (KNMI) and Germany (DWD).

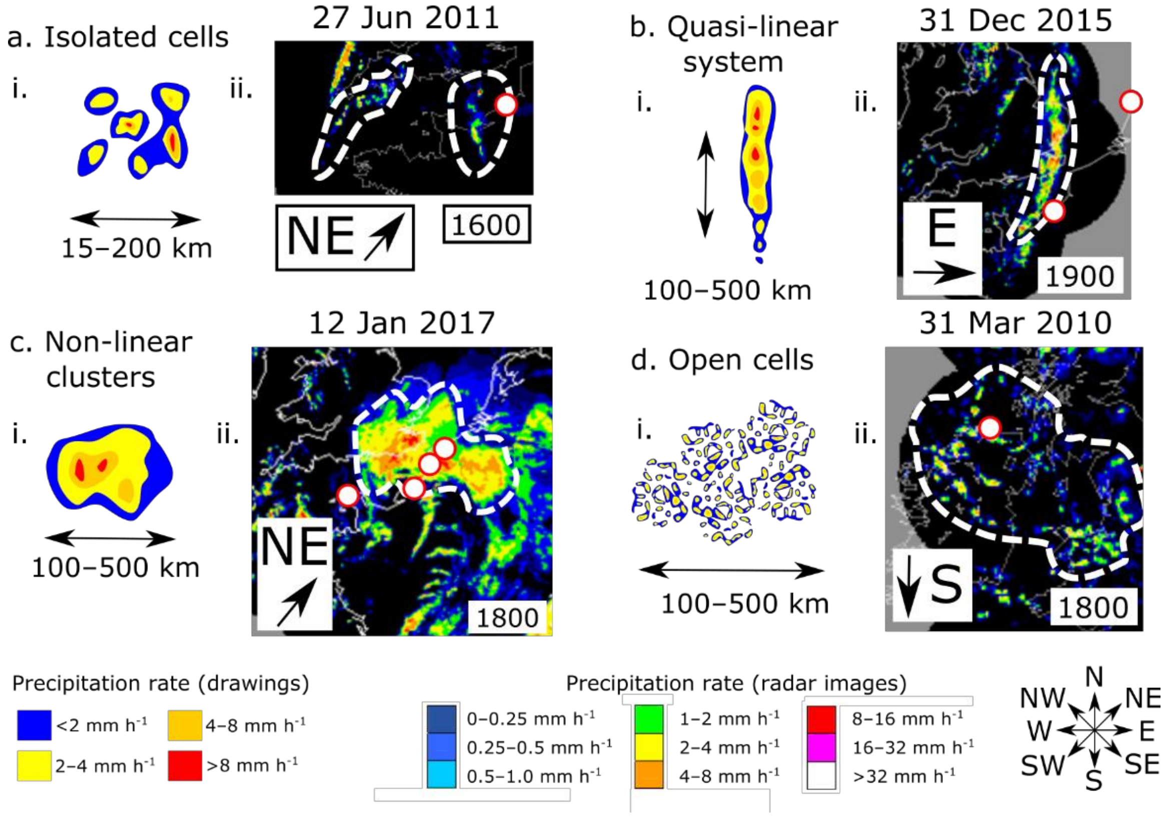

Figure 2 Classification scheme for atmospheric systems based on radar-derived precipitation and cardinal direction of overall system motion. (a) isolated cells, (b) quasi-linear systems, (c) non-linear clusters, (d) open cells. In each panel, (i) the general precipitation morphology used in classification with typical scale and simplified precipitation rate (drawings) and (ii) an example of the morphology with the tide gauges that detected a meteotsunami ≥ 0.25 m (white dots with red outlines), date, time (UTC) and cardinal direction of motion with more detailed precipitation rates (radar images) copied from the National Meteorological Library and Archive, Fact sheet No. 15.

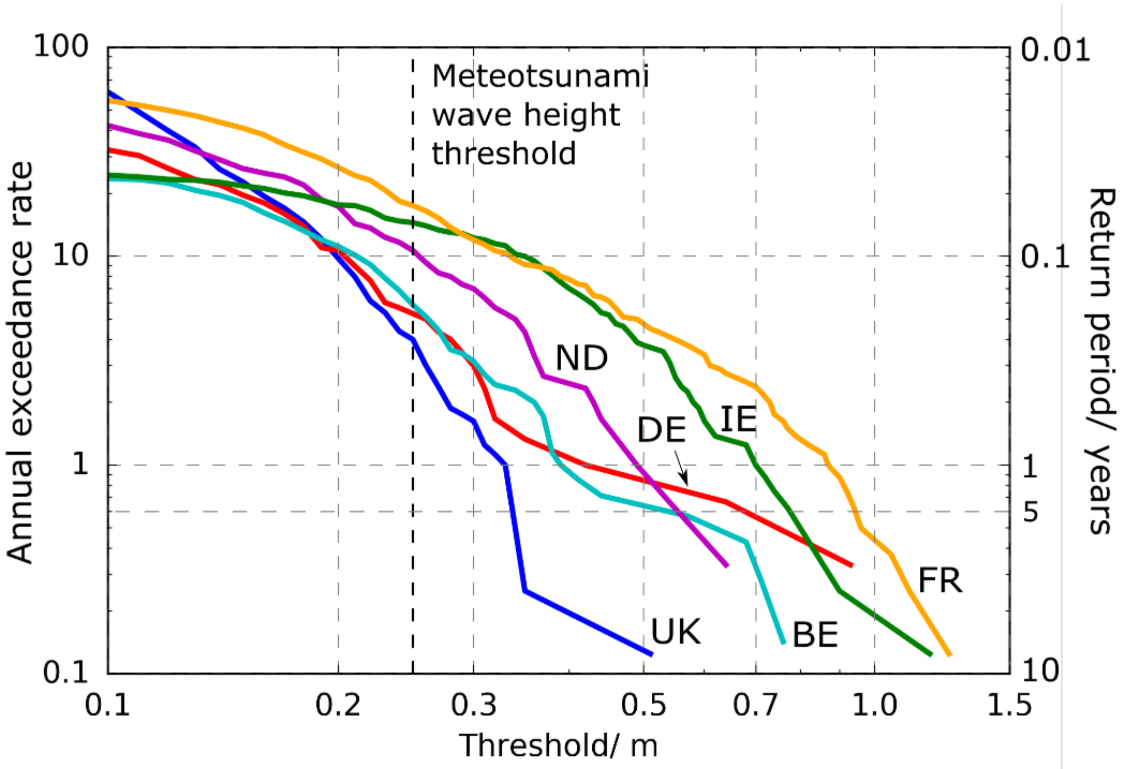

Figure 3 NSLOTT annual size-exceedance rate for thresholds between 0.1–1.5 m from tide gauges grouped across each country. IE/Republic of Ireland – green, UK/United Kingdom – blue, FR/France – orange, BE/Belgium – cyan, ND/The Netherlands – purple, DE/Germany – red. Dashed black vertical line is at 0.25 m, which is the meteotsunami wave-height threshold. Return period in years is shown on the right-hand vertical axis. A return period of *n* years indicates that on average, one NSLOTT exceeds the threshold every *n* years.

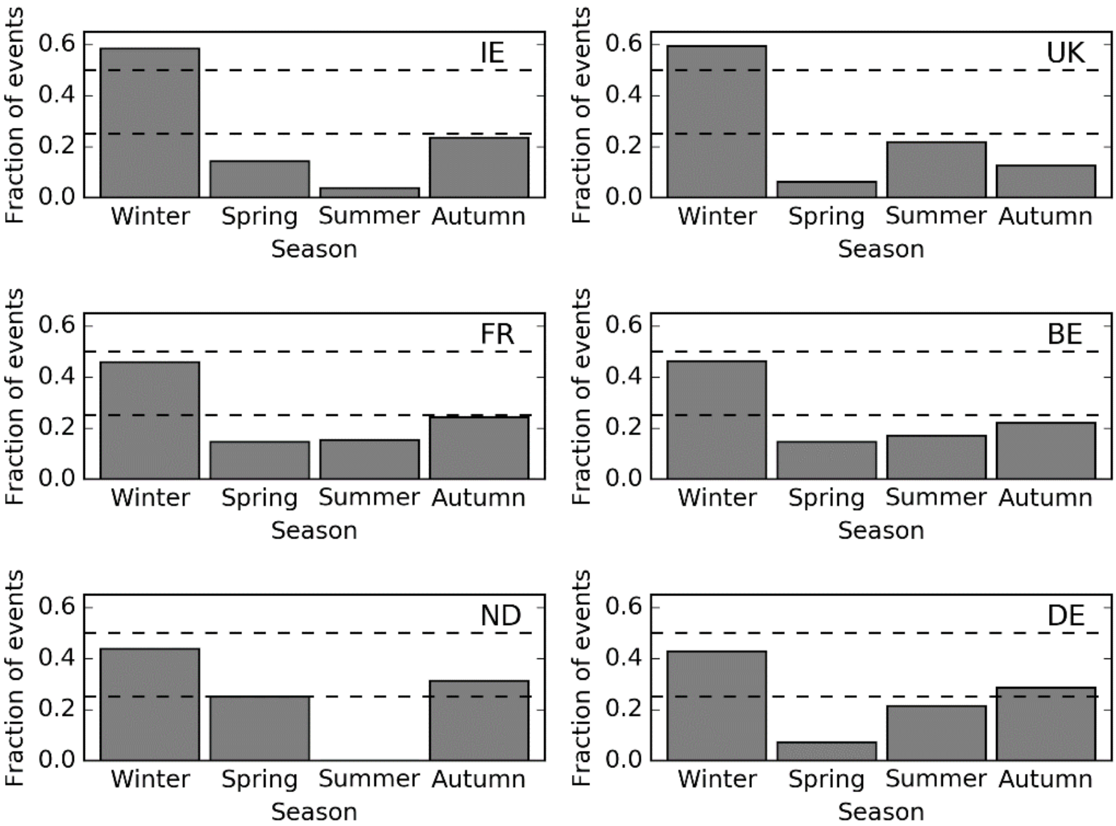

Figure 4 Seasonal variation of meteotsunamis across: (a) Republic of Ireland (IE), (b) the United Kingdom (UK), (c) France (FR), (d) Belgium (BE), (e) the Netherlands (ND), and (f) Germany (DE). Thin dashed lines at 0.25 and 0.5 for reference. Winter is defined as DJF, Spring is MAM, Summer is JJA and Autumn is SON.

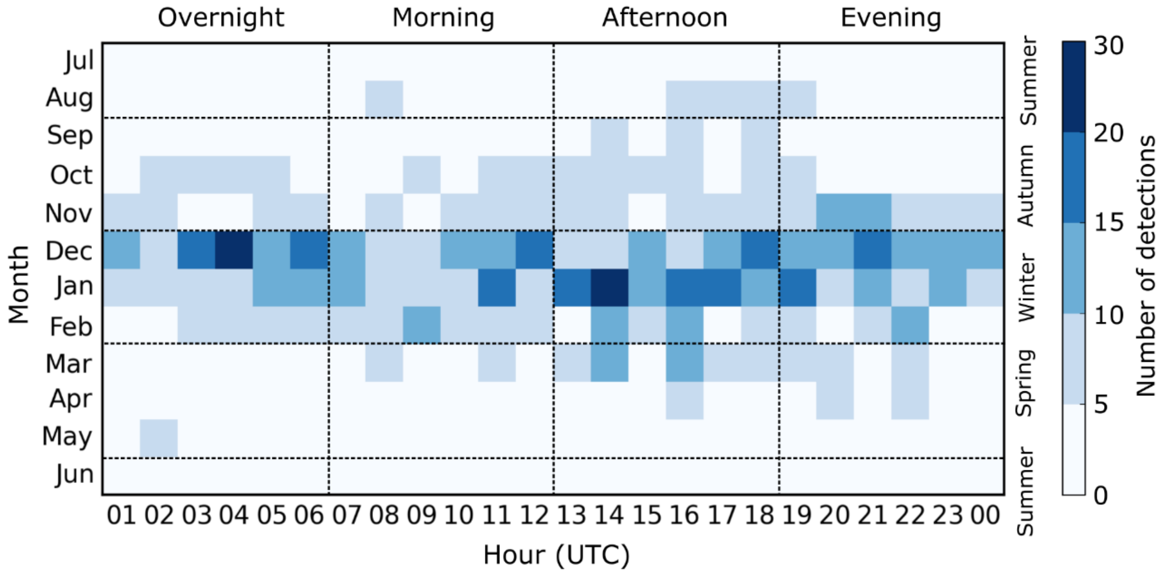

Figure 5 Seasonal and diurnal NSLOTT variation across all tide gauge stations. Number of detections are coloured according to the scale. Black dashed lines separate times of identification. Overnight was 0100–0659 UTC, morning is 0600–1159 UTC, afternoon is 1200–1859 UTC and evening is 1900–0059 UTC. Summer is JJA, Autumn is SON, Winter is DJF and Spring is MAM. Dashed lines and annotations were inserted in Inkscape.

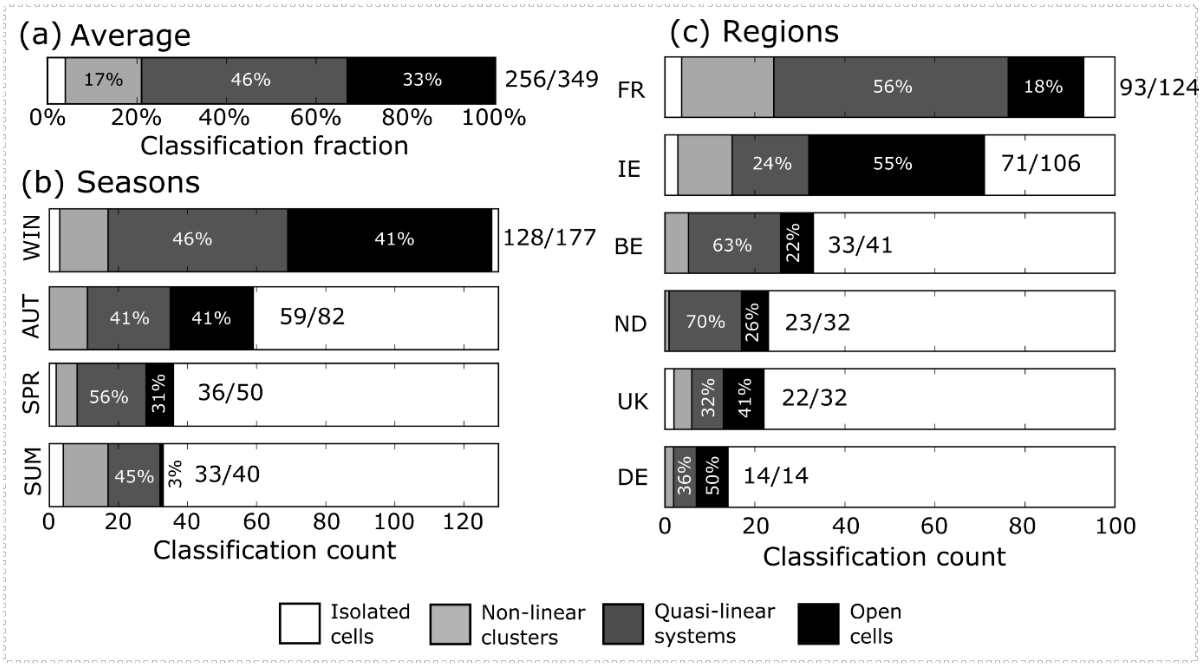

Figure 6 Fraction and count of classified events for isolated cells (white bars on left), non-linear clusters (light grey), quasi-linear systems (dark grey) and open cells (black). Results are shown for (a) the average, (b) each season (WIN = winter (DJF), AUT = autumn (SON), SPR = spring (MAM) and SUM = summer (JJA)) and (c) each country. To the right of each bar, the number of classified systems is shown compared to the total number of meteotsunamis. Countries and seasons are ordered from most classifications at the top to fewest classifications at the bottom.

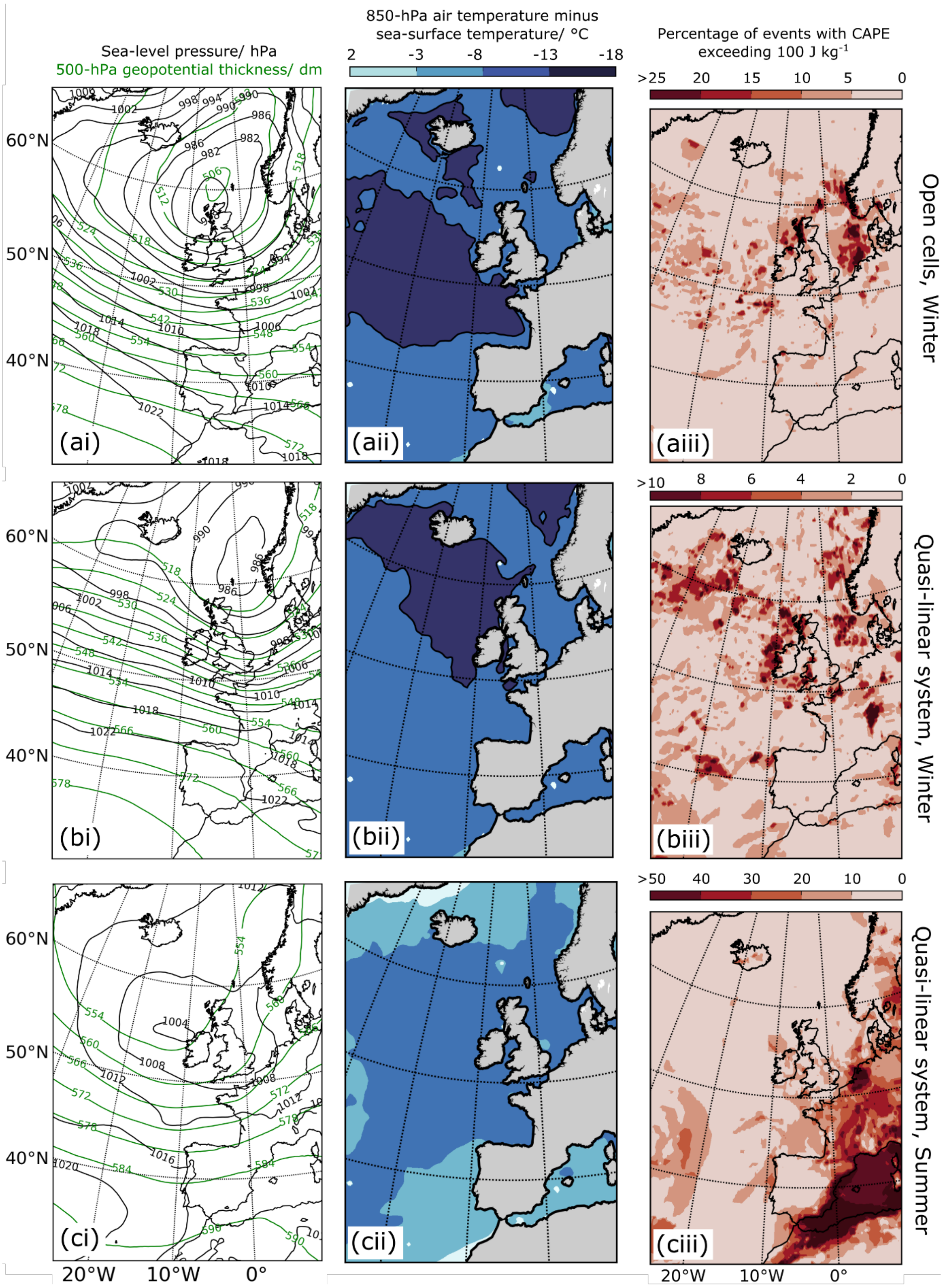

Figure 7 Synoptic composite analyses from 0.25° × 0.25° ERA5 reanalysis datasets, at the closest hour to meteotsunami detection for (a) wintertime open cells (10 meteotsunamis), (b)

wintertime quasi-linear systems (26 meteotsunamis) and (c) summertime quasi-linear systems (9 meteotsunamis). On the left, (i) shows the mean sea-level pressure (thin black lines) at 4-hPa spacing and 500-hPa height (thin green lines) at 6 dam spacing. In the middle, (ii) shows the mean of 850-hPa air temperature minus the sea-surface temperature (°C), with darker blues indicating colder air compared to the sea-surface, and a black line contour at –13°C indicating instability. On the right, (iii) shows the percentage of events with convective available potential energy > 100 J kg^{-1}. The scales for CAPE occurrence differ among (a), (b), and (c).